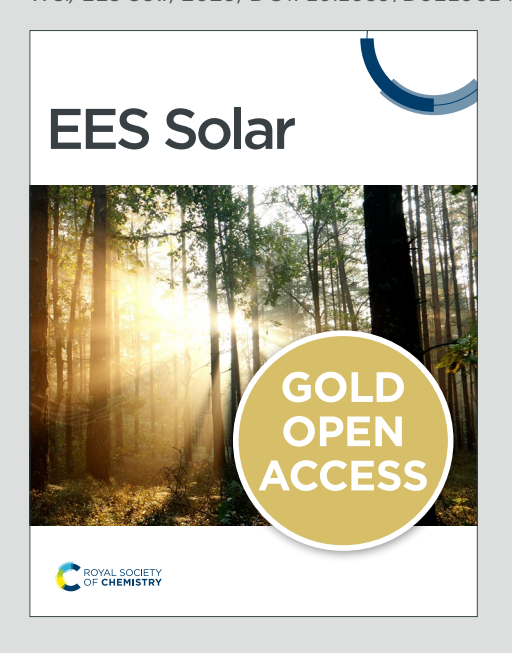




EES Solar

Accepted Manuscript

This article can be cited before page numbers have been issued, to do this please use: D. LE and T. C. Wei, *EES Sol.*, 2025, DOI: 10.1039/D5EL00143A.



This is an Accepted Manuscript, which has been through the Royal Society of Chemistry peer review process and has been accepted for publication.

Accepted Manuscripts are published online shortly after acceptance, before technical editing, formatting and proof reading. Using this free service, authors can make their results available to the community, in citable form, before we publish the edited article. We will replace this Accepted Manuscript with the edited and formatted Advance Article as soon as it is available.

You can find more information about Accepted Manuscripts in the <u>Information for Authors</u>.

Please note that technical editing may introduce minor changes to the text and/or graphics, which may alter content. The journal's standard <u>Terms & Conditions</u> and the <u>Ethical guidelines</u> still apply. In no event shall the Royal Society of Chemistry be held responsible for any errors or omissions in this Accepted Manuscript or any consequences arising from the use of any information it contains.



Open Access Article. Published on 04 nóvember 2025. Downloaded on 14.11.2025 17:54:33.

In-depth Investigation of Methylamine Gas Post-treatment for MAPbl₃ Films

View Article Online DOI: 10.1039/D5EL00143A and its Potential for Upscaling Perovskite Solar Cells

Duc-Anh Le, Tzu-Chien Wei*a,b

- Department of Chemical Engineering, National Tsing Hua University, 101, Sec.2, Guang-Fu Road, Hsinchu, Taiwan 30013, Republic of China.
 - Research Center for Critical Issues, Academia Sinica, Tainan, Taiwan, Republic of China.

Broader context

Scaling up perovskite solar cells (PSCs) for commercial applications requires maintaining high film quality over large areas, a challenge hindered by morphological defects and chemical inconsistencies. Most existing approaches to large-area fabrication involve modifying the drying process - such as using co-solvents or alternative techniques - to improve film uniformity. While these methods enhance film, quality compared to small-area antisolvent processes, they still result in performance losses during scale-up, indicating that a truly lossless transition to large-area devices has not yet been achieved. We propose that a more practical and effective solution lies in post-treatment strategies that repair or modify films after deposition to homogenize morphology and composition. Among these, methylamine gas treatment (MATM), which induces film liquefaction and recrystallization, shows particular promise. This method offers the potential to enhance film uniformity and preserve device efficiency during scaling. In our earlier research, we demonstrated control of MATM through adsorption kinetics and developed a prototype reactor capable of uniformly treating substrates as large as 10 cm × 10 cm, laying the groundwork for scalable, efficiencyretaining fabrication of perovskite films.

Solar Accepted Manus

View Article Online DOI: 10.1039/D5EL00143A

ARTICLE

In-depth Investigation of Methylamine Gas Post-treatment for MAPbI₃ Films and its Potential for Upscaling Perovskite Solar Cells

Received 00th January 20xx, Accepted 00th January 20xx

DOI: 10.1039/x0xx00000x

Duc-Anh Le, a Tzu-Chien Wei*a,b

Scaling up perovskite solar cells (PSCs) for commercial applications requires maintaining film quality across large areas, a challenge often compounded by morphological defects and chemical heterogeneity. Methylamine gas treatment (MATM) offers a promising post-processing strategy by inducing liquefaction and recrystallization of Methylammonium-based perovskite films, thereby enhancing their uniformity and chemical homogeneity. However, how to properly conduct the MATM-particularly the influence of environmental humidity on its outcome has rarely been investigated. In this study, we report that environmental moisture critically undermines MATM efficacy by triggering side reactions that generate PbO, PbIOH, and MAPbI₂OH impurities. Through systematic comparison of MAPbI₃ films treated under dry and humid conditions, we elucidate the degradation mechanisms using various analyses and conclude moisture exposure during MATM drastically increases trap densities and non-radiative recombination, leading to reduced carrier lifetimes and photovoltaic performance. A PSC with an initial power conversion efficiency (PCE) of 16.67% exhibits a significant improvement to 19.48% after undergoing MATM in a dry environment. In contrast, when MATM is performed under humid conditions, although the surface smoothness of the MAPbI₃ film is greatly improved, the PCE of the device declines instead of increasing. This outcome highlights the detrimental effects of side reactions induced by moisture during the MATM process. These findings underscore the importance of moisture isolation in MATM to enable the reliable upscaling of high-efficiency and stable perovskite solar modules.

Introduction

Organic lead halide perovskites (PVSKs) have garnered significant attention in recent years as absorbers for photovoltaic devices due to their low exciton binding energy, high extinction coefficient and exceptional defect tolerance¹⁻⁵. Since Miyasaka's group first reported perovskite solar cells (PSCs) based on these materials in 2009, their power conversion efficiency (PCE) has sharply increased to 27.0%, rivalling that of crystalline silicon photovoltaic technology, which has been developed for over half a century^{6, 7}. Despite this impressive progress, such high PCE PSCs were achieved primarily on very small active areas (mostly <0.1 cm²). However, in practical applications, the performance of photovoltaic devices is evaluated by power output rather than efficiency alone. Thus, the ability to maintain high PCE over large-area substrates has become a critical challenge in the commercialization of PSCs. An ideal PVSK layer should exhibit a homogeneous chemical Despite the promising results achieved with small-area devices, the application of these techniques to large-area substrates remains technically challenging, particularly in terms of uniform film formation, defect control, and process reproducibility. Various methods for fabricating large-area perovskite absorber layers have been reported, among which solution-based, wetcoating processes remain the most mature and widely applied. These approaches involve dissolving perovskite precursors in highly polar organic solvents, coating them onto substrates to form wet films, and then inducing crystallization by removing the solvent. Based on a literature survey on large-area PVSK thin film fabrication, the process can be generally divided into three

Step-1: deposition of the wet precursor film, using methods such as spin coating⁸, slot-die coating⁹, spray coating^{10, 11}, screen printing¹², and inkjet printing¹³;

Step-2: drying and crystallization to form a primary PVSK film, using techniques such as anti-solvent treatment $^{14, 15}$, thermal annealing 16 , vacuum-assisted drying $^{17, 18}$, or hot wind drying $^{19, 20}$.

Step-3: post-treatment to further improve PVSK film quality, such as passivation, solvent annealing²¹⁻²³or liquefaction–recrystallization strategies^{24, 25}.

It is worth noting that in many reports on large-area PSCs, the precursor solution used in Step-1 is often supplemented with a secondary solvent or specific additives to modulate the

composition, a compact and smooth morphology, and low impurity content. After more than a decade of effort, these

properties can now be reliably achieved in small-area devices.

^a Department of Chemical Engineering, National Tsing Hua University, 101, Sec.2, Guang-Fu Road, Hsinchu, Taiwan 30013, Republic of China.

b. Research Center for Critical Issues, Academia Sinica, Tainan, Taiwan, Republic of China.

[†]Supplementary Information available. See DOI: 10.1039/x0xx00000x

cen Access Article. Published on 04 nóvember 2025. Downloaded on 14.11.2025 17:54:33.

ARTICLE EES Solar

crystallization behaviour and improve the morphology and quality of the resulting PVSK films²⁶⁻²⁹ Among these three steps, we believe that Step-3, the post-treatment stage, is particularly critical for future large-scale production, as it possibly provides a "healing" mechanism to fix the quality of the primary PVSK film formed in Step-2, if it is properly designed. This, in turn, reduces the precision demands and investment on both the coating equipment and the solvent removal systems, which can have a positive impact on lowering manufacturing costs and improving production yield.

The liquefaction-recrystallization strategy is one typical example for Step-3, it involves reacting the primary PVSK film (formed after Step-2) with amine compounds to produce a chemically adsorbed intermediate in a liquid phase. This liquid intermediate allows for self-levelling of the film, and upon removal of the amine species, a recrystallized PVSK film (hereafter named as secondary PVSK) with enhanced uniformity and compactness can be obtained. A representative showcase of this strategy is the methylamine gas treatment (MATM) for MA-based perovskites. Methylamine (MA⁰) is a volatile chemical (boiling point -6 °C) that can rapidly react with MAPbI₃, inducing liquefaction of the perovskite layer within less than one second. Subsequent removal of MA⁰ leads recrystallization, enhancing crystal quality and reducing defect density, thereby improving PSC performance ^{24, 25, 30-33}.

MATM was first proposed by Pang et al. in 2015, who attributed the liquefaction-recrystallization mechanism to interactions between the lone electron pair on the nitrogen atom of MA⁰ and the PbI₆ octahedra in MAPbI₃, disrupting the 3D crystal structure and resulting in liquefaction. Other studies have shown that PbI₂, a common precursor in perovskite formation, can also transit into a molten state upon exposure to MA⁰ or other amines, suggesting that the liquefaction is driven by coordination between Pb2+ ions and amines24, 25, 30, 34-37. Kerner et al. further reported that the formation of Pb-amide bonds via proton transfer plays a critical role in triggering the liquefaction³⁸.

As noted above, the adsorption and desorption kinetics in MATM are extremely rapid, with the liquefaction occurring within ~1 second³². This narrow process window poses a major challenge for implementing MATM in scalable manufacturing systems. To address this issue, we have developed a controllable MATM technique in which the partial pressure of MA⁰ is finely tuned to control the liquefaction kinetics. We have found that the amount of MA⁰ adsorbed onto the primary MAPbl₃ film significantly influences the morphology and crystallinity of the resulting secondary film. Moderately reducing the MA⁰ concentration during MATM facilitates the formation of high-quality films. Using our home-made MATM chamber, we successfully scaled up the process from small-area devices to 5 cm × 5 cm mini-modules without PCE loss³¹.

To further evaluate the industrial feasibility of MATM, this study investigates the influence of environmental moisture during treatment, as humidity content is an important factor in PSC fabrication. In 2020, Bogachuk et al. reported that MA⁰ reacted with MAPbI₃ powders in humid environments to form photoinactive by-products such as PbIOH, demonstrating that moisture can significantly hinder successful recrystallization during MATM³⁹. Controlling humidity auring 1970 authoring humidity closely tied to manufacturing cost. Therefore, humidity not only affects the outcome of MATM but also represents a critical consideration in the design of future PSC production lines. Based on this background, this study systematically examines the effect of ambient humidity on the crystallinity, morphology, and optoelectronic properties of secondary MAPbI₃ films treated with MA⁰. We further correlate these findings with device performance, stability, and reproducibility, in order to strengthen the feasibility of this method for future large-scale PSC manufacturing.

Experimental section

Substrate cleaning

The fluorine doped tin oxide glass (FTO, 2.2 mm thick, 8 Ωsq⁻¹, Dyesol) was dried etching by laser machine (LMF-020F, Laser Life Company, Taiwan). The etching FTO was cleaned by detergent solution (PK-LCG46, Parker International Co. Ltd., Taiwan) and reverse osmosis (RO), then rinsed with deionized water (DI), ethanol 95% (ECHO, Taiwan), and dried by hot-air blow gun. Before compact layer TiO2 (cTiO2) deposition, the cleaned FTO substrate was treated by UV/Ozone for 30 min.

Electron transport layer (ETL)

The cTiO₂ precursor solution was prepared by mixing 6% v/v of titanium diisopropoxide bis(acetylacetonate) solution, 4% v/v of acetylacetonate and ethanol. The cTiO₂ precursor was sprayed on hot reheated FTO for 8 circles. In which, the flow of O₂ was controlled at 0.4 L/min, and 1 min resting time for each circle. After spraying process, the substrates were annealed at 500 °C for 30 min.

A commercial paste TiO₂ (30 NR-D, GreatcellSolar) was diluted in ethanol absolute 99.8% (Honeywell) with ratio 1:7 (weight). Then it was coated onto the cTiO₂ substrate at 6000 rpm for 30 s. Mesoporous TiO₂ (msTiO₂) coated substrate was dried on the 120 °C hotplate for 5 min, then the msTiO₂ films were gradually to 500 °C and cooled to room temperature. After cooling down to $150\,^{\circ}\text{C}$, the msTiO₂ substrate was treated by UV-Ozone for 20 min, then transferred to humidity-controlled room (10-20% humidity) for preparation of perovskite films.

PVSK fabrication

A PVSK precursor solution contains 1.5 M PbI₂ (99.0%, Xian Polymer Chemicals) 1.5 M MAI (GreatcellSolar) and 0.35 M MACI (99.9%, GreatcellSolar) in DMF:DMSO (99.9%, Sigma-Aldrich) mix solvent (volume ratio = 9:1). Primary-MAPbl₃ films were prepared by coating the precursor solution onto msTiO₂ substrate at 3000 rpm for 10 s, then the wet PVSK film was transferred to a vacuum chamber with continuous N₂ flow. The pressure of chamber was controlled at 150 torr, and the PVSK film was in vacuum for 30 seconds. After that, the dried PVSK film was heated at 150 °C for 10 min.

MATM under various moisture conditions

A MA⁰ induced liquefaction and recrystallization reactor (MALCR) was used to prepare MA0-treated MAPbI3 films (2nd-

ARTICLE

as above. The PVSK coating followed the coating process using

MAPbl₃/dry). MA⁰ gas was generated from a 33 wt% MA⁰ ethanol solution (Sigma-Aldrich). The effective concentration was determined using Raoult's law, and the measured vapor pressure (149 kPa) corresponded to ~45% MA⁰ concentration during MATM. The Primary-MAPbI₃ films were moved into the MALCR system and vacuum for 5 min to remove moisture absorption on PVSK films. Then MA⁰ gas was expose into the reaction chamber. At the point during exposure where the PVSK completely changes to transparent (a few seconds), the MALCR chamber was vacuum to remove MA⁰ gas. The transparent film was changes back to the dark brown film. Then the pressure was released and the 2nd-MAPbI₃/dry films were moved onto the 100 °C hotplate for 10 min to completely remove remaining MA⁰ gas on the PVSK films.

For the MATM in the presence of moisture, the MA⁰ gas was premixed with air from a controlled dry room (25 °C, 20% RH) before injection into the MALCR. Thus, the chamber humidity was maintained consistently at 20% RH throughout the treatment for 5 minutes. 2nd-MAPbl₃/wet films were then obtained after evacuating the chamber to complete the desorption process. 2nd-MAPbI3/wet/heat films prepared by heating the 2nd-MAPbI3/wet films at 100 °C for 5 min.

After cooling down to room temperature, the **2nd-MAPbl**₃ films were moved back to the humidity-control room to be deposited hole transporting material (HTM).

Hole transporting layer (HTL) deposition

precursor containing 32 mM Lithium bis(trifluoromethanesulfonyl)imide (Li-TFSI, >99.9%, Sigma-Aldrich), and 195 mM 4-tert-Butylpyridine (4-tBP, 96%, Sigma-Aldrich) in CB was kept stirring in room temperature for 1 day. 2,2',7,7'-Tetrakis[N,N-di(4-methoxyphenyl)amino]-9,9'spirobifluorene (Spiro-OMeTAD, 99.5%, Lumtec) powder was added into The HTM precursor (75 mM) as the HTM solution. The HTM solution was spin-coated onto the FTO/ETL/Perovskite substrate at 4000rpm for 25s. Then, the pre-mature devices (FTO/ETL/PVSK/HTL) were stored at a dark and dry box (RH = 10%) overnight.

Electrode deposition

An ~100nm thickness gold electrode was thermally evaporated onto the HTL at 1×10-6 mbar.

Module fabrication

The FTO glass was cut as 4 cm x 4 cm or 5 cm x 5 cm then was scribed P1 by laser machine with 532 nm Laser (Lifelaser. Co. Ltd). The laser speed, power ratio and frequency were 300 mm/s, 40% and 20 kHz, respectively. The etching FTO was cleaned by following the substrate cleaning process. Before spraying cTiO₂, the clean FTO was cleaned under UV-O₃ for 30 min then reheated at 500 °C for 30 min and kelp at 500 °C during spraying process.

The cTiO₂ and msTiO₂ coating were following the spray-coating compact layer and spin-coating mesoporous layer above. After annealing msTiO₂ and cooling down to 150 °C, the TiO₂ substrate was treated by UV-Ozone for 30 min, then transferred to humidity-controlled room (10-15% humidity) for preparation of PVSK films. The PVSK precursor was prepared 1.5 M MAPbI₃

DOI: 10.1039/D5EL00143A vacuum method.

The MATM was operated by using the home-made MALCR as the 2nd-MAPbl₃/dry film preparation. The MA solution (33 wt.% in absolute ethanol) was stored in MA⁰ source chamber. Another chamber was used as reacting chamber. The reacting chamber was vacuum drawn to reach around 8 torr on sensor. Then the valve, which connected the MA⁰ source chamber and reacting chamber, was slowly opened until the pressure value on sensor reached 150 Torr. The N2 flow and vacuum pump were used to purge MA⁰ gas out of the MATM chamber. Then PVSK films were heated at 100 °C for 10 min.

The pre-solution containing 16 mM Li-TFSI, and 85 mM 4-tBP in CB was kept stirring in room temperature for 1 day. The Spiro-OMeTAD powder was added into the pre-solution (35.5 mM) as the HTM solution. The HTM solution was spin-coated onto the perovskite film at 2000 rpm for 25 s.

Then, the pre-mature devices (FTO/ETL/Perovskite/HTL) were scribed P2 by laser with 100% power ratio, 70 kHz in frequency and 1800 mm/s speed of laser. Then the pre-mature devices stored at a dark and dry box (RH = 10%) overnight.

An ~100nm thickness gold electrode was thermally evaporated onto the HTL at 1×10⁻⁶ mbar. Finally, P3 etching used at the same laser with P2 with laser power ratio of 100%, frequency of 80 kHz and 1800 mm/s.

Characterization

The surface morphology of the samples was examined using field-emission scanning electron microscopy (FESEM, HITACHI, Japan), while atomic force microscopy (AFM, C3000 Nanosurf, Switzerland) was employed to assess surface roughness. The optical properties were characterized through ultravioletvisible (UV-Vis) spectroscopy using a spectrometer (UV-vis HP8453, USA). Steady-state and time-resolved photoluminescence (PL and TRPL) measurements were conducted with a photoluminescence spectrometer (FS5 EDINBURGH Instrument, England). Structural analysis of the thin-film samples was performed via X-ray diffraction (XRD) using a Brucker 8D X-ray diffractometer, equipped with a ceramic tube (Cu K α , λ = 1.5418 Å). X-ray photoelectron spectroscopy (XPS, PHI 5000 Versa Probe II, USA) was applied to investigate the chemical state of different types of PVSK and Pbl₂ films. The photovoltaic performance of was evaluated using a computer-controlled digital source meter (Keithley 2401, USA) under simulated sunlight provided by a commercial solar simulator (PEC-L15, Percell Technologies, Japan) at 1 sun, AM1.5G, with light intensity calibrated by a monocrystalline silicon photodiode (KG3, Oriel, USA). A 0.056 cm² photomask was affixed to the front of the PSC to ensure precise control over the illuminated area for small-scale devices. Additionally, the trap-filled limit voltage (V_{TFL}) was determined through space charge limited current (SCLC) measurements using a digital source meter (Keithley 2401, USA), employing a scanning rate of 10 mV/s within a voltage range of 0 to 4 V

Results and discussion

Open Access Article. Published on 04 nóvember 2025. Downloaded on 14.11.2025 17:54:33.

ARTICLE EES Solar

Chemical reaction of MAPbl₃ /Pbl₂ and MA⁰ in moisture.

Four types of MAPbI₃ films were investigated in this study, including the primary MAPbI₃ film (**Primary-MAPbI₃**) used as a control and three secondary MAPbI₃ films subjected to different MATM conditions. All MATM processes were carried out in a home-made, custom-designed methylamine liquefaction and crystallization reactor (MALCR, shown in **Figure S1**), which features a dual-function chamber that allows for either vacuum evacuation or methylamine treatment to be conducted independently. The first secondary MAPbI₃ sample (**2nd-MAPbI₃/dry**) was prepared by placing the primary MAPbI₃ film into the MALCR chamber, followed by a 10-minute vacuum treatment to re move moisture from both the film surface and the chamber interior. Afterward, MATM was performed to

ensure that the reaction occurred in a moisture-free environment. Following this, the chamber was occurred in a moisture-free environment. Following this, the chamber was occurred at the desorption process. This sample is hereafter named as the 2nd-MAPbi₃/wet. For the third secondary MAPbi₃ sample, after undergoing the same MATM process as the previous sample, the film was further heated on a 100 °C hotplate for 10 minutes after removal from the chamber, this sample is hereafter named as 2nd-MAPbi₃/wet/heat. The sample preparation flowchart is illustrated in Figure 1.

Firstly, crystallinity and phase composition of the investigated MAPbI₃ films was analysed using XRD. The XRD patterns are collected and shown in **Figure 2a**. Crystallographic reference data were obtained from the following databases: tetragonal MAPbI₃ (COD-4518042)⁴⁰, PbO.PbIOH (COD-9017630), PbIOH

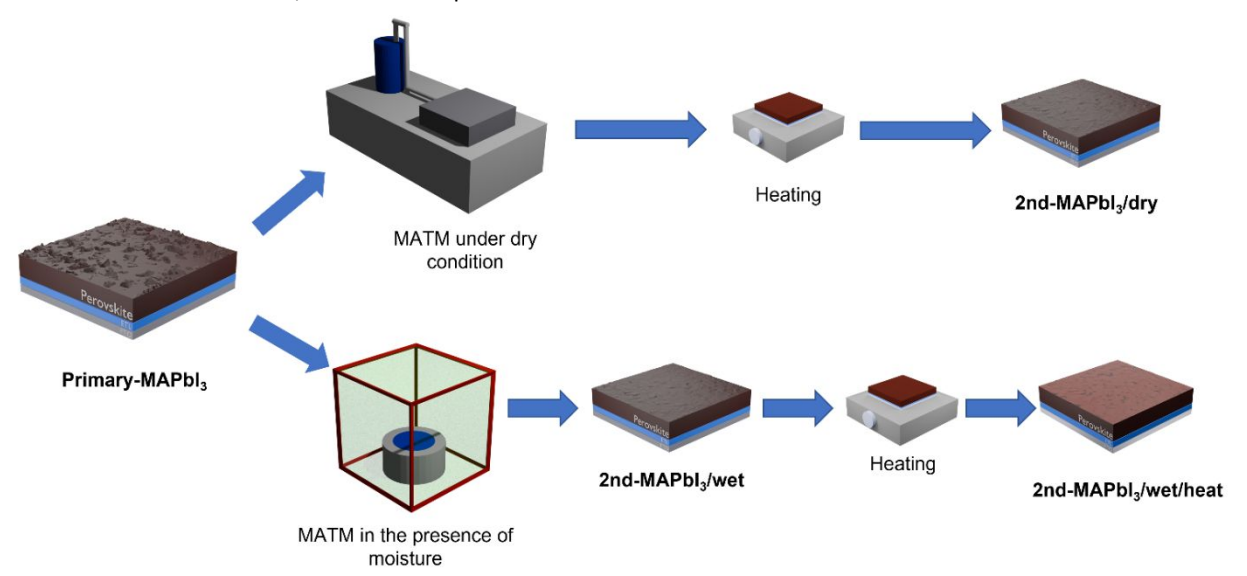


Figure 1: Schematic diagram of sample preparation

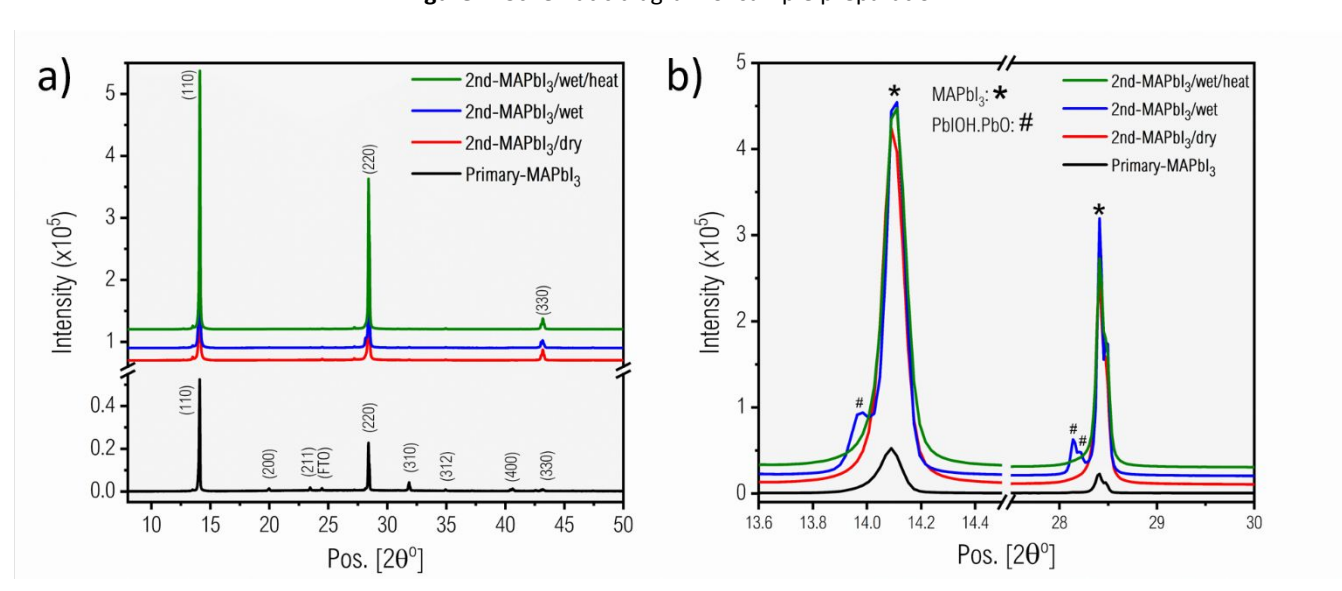


Figure 2: a) XRD pattern and b) zoom-in peak at 14.0° and 28.5° of Primary-MAPbI₃, 2nd-MAPbI₃/dry, 2nd-MAPbI₃/wet and 2nd-MAPbI₃/heat films

Solar Accepted Manuscri

EES Solar ARTICLE

(COD-9017629)41, PbO (COD-9012703)42, and PbI₂ (COD-9009141)⁴³, which were used to identify the formation of the main perovskite phase and possible impurity phases. Primary-MAPbl₃ exhibits characteristic diffraction peaks at 2θ values of 14.09°, 19.98°, 23.47°, and 28.43°, corresponding to the (110), (200), (211), and (220) planes of polycrystalline MAPbI₃, respectively. In contrast, the three secondary MAPbI₃ samples display three prominent diffraction peaks at 14.10°, 28.39°, and 43.23°. Notably, the peak corresponding to the (110) plane ($^{\sim}2\theta$ = 14°) is significantly enhanced – by approximately one order of magnitude-consistent with previous reports^{25, 31, 35, 44}. Zoom-in XRD pattern of the 2nd-MAPbI₃/wet (Figure 2b) shows extra diffraction peaks at $2\theta = 13.94^{\circ}$, 28.13° , and 28.33° , which are attributed to PbO.PbIOH, clearly indicating that the presence of moisture during the MATM process can lead to the formation of impurity. This observation is in agreement with the findings reported by Bogachuk et al.³⁹. Although these impurity-related diffraction peaks disappeared 2nd-MAPbI₃/wet/heat, further investigation is necessary to confirm whether the impurities have been eliminated.

The XPS survey spectrum (Figure S2) of a MAPbl₃ perovskite film reveals peaks at binding energies of 532 eV, 402.5 eV, and 285 eV, corresponding to O 1s, N 1s, and C 1s orbitals, respectively. The characteristic doublet peaks of Pb 4f and I 3d are observed at approximately 138 eV/143 eV and 619 eV/631 eV, respectively, with their expected spin-orbit splitting. To study the chemical modifications in MAPbI₃ films under moisture exposure, XPS elemental spectra were analysed. The spectra were calibrated to 285.0 eV, referencing the C 1s binding energy associated with adventitious (aliphatic) carbon or surfaceadsorbed hydrocarbon species from the atmosphere⁴⁵. The core-level spectra were fitted using Gaussian line shapes with a Shirley background to ensure accurate peak deconvolution. Figure S3a displays the XPS spectra of the C 1s core level of investigated samples. All of them exhibit five peaks at 285.0 eV, 286.4 eV, and 286.7 eV. The peak at 285.0 eV is used for calibration and is attributed to adventitious carbon or surfaceadsorbed hydrocarbon species. The peak at 286.4 eV can be assigned to C-O or C-OH, which is also associated with surfaceadsorbed species. The peak at 286.5 eV can be attributed to C-N bond of ammonium species in the MAPbI₃ film. Figure S3b shows the XPS of N 1s core level of MAPbI₃ films. All samples contain a single peak at 402.5 eV, corresponding to the C-N bond in MAPbI₃ films. The XPS spectra for core level I 3d (Figure S3c) exhibit two peaks at 619.4 eV and 630.8 eV, corresponding to doublets I $3d_{5/2}$ and I $3d_{3/2}$, which are assigned to Pb-I bonding in MAPbI₃ film.

Figure 3 shows Pb 4f core level spectra of investigated MAPbI₃ films. Primary-MAPbI₃ (Figure 3a) and 2nd-MAPbI₃/dry (Figure 3b) exhibit nearly identical spectra, in which the Pb $4f_{7/2}$ peaks can be further deconvoluted to two contributions at 138.5 eV and 136.8 eV, corresponding to Pb-I, and metallic lead (Pb⁰), respectively. For 2nd-MAPbI₃/wet (Figure 3c)and 2nd-MAPbI₃/wet/heat(Figure 3d), the Pb $4f_{7/2}$ spectra exhibit a positive shift, allowing for the fitting of an additional peak at

approximately 138.7 eV, which is attributed to Physical P zoom-in observation (Figure S4) of 136.0 Po 138.0 Po 138. Pb $4f_{7/2}$ spectra reveals the existence of an additional peak at 137.1 eV for 2nd-MAPbl₃/wet and 2nd-MAPbl₃/wet/heat, which is attributed to Pb-O⁴⁷. Figure 4 depicts the binding ratios from deconvoluted Pb 4f_{7/2} spectra. In **Primary MAPbI₃**, Pb-I bonding characteristic of MAPbI₃ accounts for as much as 95.3% of the total lead signal, with the remaining 4.7% consisting of Pb⁰. Notably, contributions from Pb–OH and Pb–O species are not detectable. The result for 2nd-MAPbl3/dry is similar to those of Primary-MAPbI₃, with contributions from Pb-I, Pb⁰ accounting for 96.7%, and 3.3% respectively. This strongly supports the conclusion that MATM conducted in a dry condition, specifically repairs film morphology without altering the chemical composition of the MAPbI₃ layer. On the contrary, in 2nd-MAPbl₃/wet, the proportion of Pb-I bonds decrease sharply to 56.6%, accompanied by a significant increase in Pb-OH and Pb-O signals to 41.6% and 1.4%, respectively. This clearly confirms the catastrophic chemical transformation that occurs when MATM is conducted in a humid environment: nearly one-third of the MAPbI₃ is converted into photoinactive by-products. For 2nd-MAPbl₃/wet/heat, the contributions of Pb-I, Pb-OH, and Pb-O are 60.6%, 36.6%, and 2.8%, respectively. These results indicate that post-heating fails to remove the degradation products formed during the moistureinvolved MATM. In fact, the Pb-O signal slightly increases, suggesting further chemical transformation during the heat treatment. This strongly implies that the Pb-OH species in the 2nd-MAPbl₃/wet are not merely in the form of Pb(OH)₂, but rather exist as photoinactive MAPbI_{3-y}(OH)_y-type pseudoperovskites.

Based on the XPS analysis, we propose the following reaction mechanism when MATM undergoes in the presence of moisture. Ideally, MA 0 gas is absorbed onto the MAPbI $_3$ film, inducing a liquid-phase transition to MAPbI $_3 \cdot x$ MA 0 :

$$\chi MA^0_{(gas)} + MAPbI_{3 (solid)} \rightarrow MAPbI_{3} \cdot \chi MA^0_{(liquid)}$$
 (1)

When moisture exists, the unpaired electron on the nitrogen atom of MA^0 readily interacts with H_2O , leading to the formation of MAOH:

$$MA_{(gas)}^0 + H_2O_{(gas)} \rightarrow MAOH_{(gas)}$$
 (2)

Water can also react with adsorbed MA⁰ to form MAOH-related intermediates:

$$MAPbI_3 \cdot xMA^0_{(liquid)} + xH_2O_{(gas)} \rightarrow MAPbI_3 \cdot xMAOH_{(liquid)}$$
(3)

The OH⁻ then exchanges with the I⁻ in the liquid intermediate, leading to the formation of MAPbl_{3-v}(OH)_v intermediate:

$$MAPbI_3 \cdot xMAOH_{(liquid)} \rightarrow MAPbI_{3-y} (OH)_y \cdot (x-y)MAOH_{(liquid)} + yMAI_{(solid)}$$
 (4)

This intermediate can further degrade into PbIOH and PbO:

Open Access Article. Published on 04 nóvember 2025. Downloaded on 14.11.2025 17:54:33.

ARTICLE EES Solar

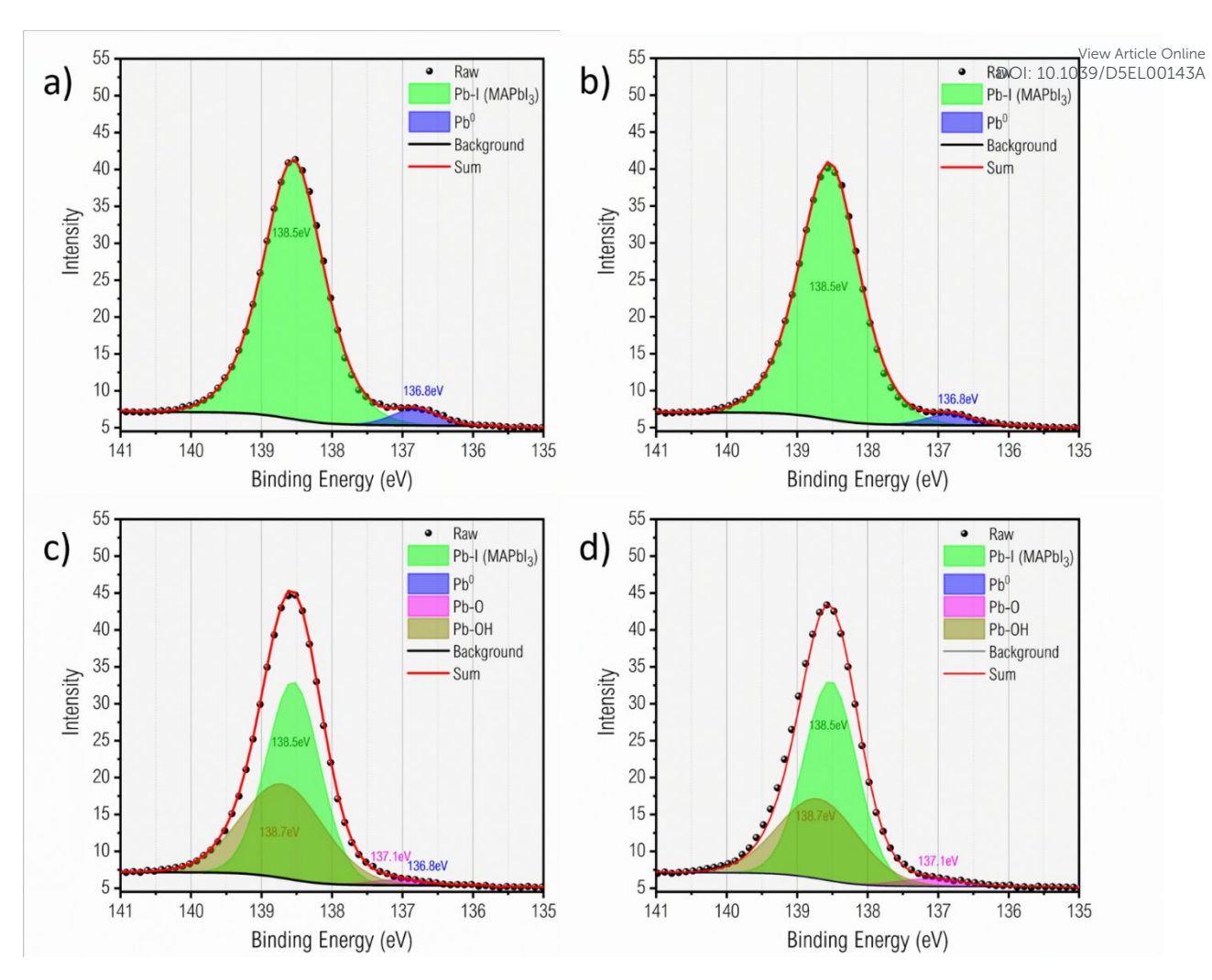


Figure 3: XPS Pb 4f_{7/2} region of a) Primary-MAPbI₃, b) 2nd-MAPbI₃/dry, c) 2nd-MAPbI₃/wet and d) 2nd-MAPbI₃/heat films

$$MAPbI_{3-y}(OH)_y \cdot (x-y)MAOH_{(liquid)} \rightarrow$$

 $MAPbI_{3-y}(OH)_{y(solid)} + (x-y)MAOH_{(gas)}$ (5)

$$MAPbI_{3-y}(OH)_{y(solid)} \rightarrow yMAI_{(solid)} + yPbIOH_{(solid)} + (1-y)MAPbI_{3(solid)}$$
 (6)

$$2PbIOH_{(solid)} \rightarrow 2PbO_{(solid)} + H_2O_{(gas)}$$
 (7)

Since solution-processed MAPbl₃ films typically contain unreacted Pbl₂⁴⁸⁻⁵⁰, we then shifted our focus on the effect of Pbl₂ during moisture-involved MATM. Whether and how this residual Pbl₂ undergoes transformation during the MATM process remains an intriguing yet explored question. Following the same analytical approach used for MAPbl₃, we prepared three types of Pbl₂ film samples: Raw-Pbl₂, Pbl₂/wet, and Pbl₂/wet/heat. These correspond to Pbl₂ films spin-coated onto glass substrates, films subjected to moisture-involved MATM, and those further treated by post-annealing, respectively. Figure 5 presents the XRD patterns of the investigated Pbl₂ samples, in which the diffraction pattern of Raw-Pbl₂ displays characteristic peaks at 12.68°, 22.99°, 25.45°, 33.66°, 39.54°, and 41.70°, corresponding to (001), (010), (002), (120), (121)

orientations of Pbl_2 polycrystals. For Pbl_2 /wet, additional peaks emerge at 14.11°, 28.39°, 31.87°, 40.80°, and 43.26°. Notably, the peak at 14.11° closely aligns with the (110) characteristic diffraction of MAPbl₃, strongly implying the formation of

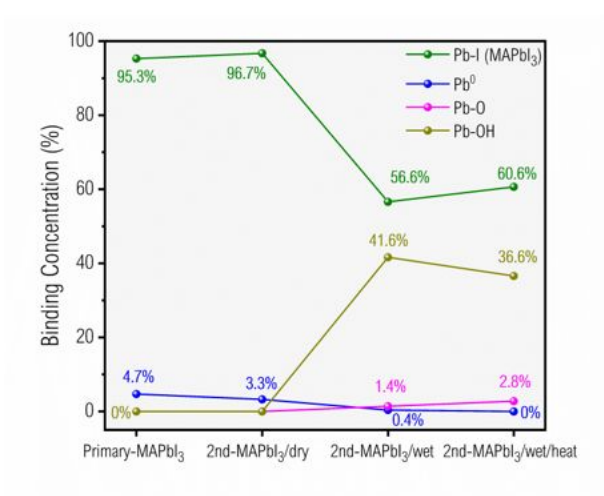


Figure 4: Pb binding ratios of four types MAPbI₃ films from deconvoluted Pb 4f_{7/2} spectra.

Open Access Article. Published on 04 nóvember 2025. Downloaded on 14.11.2025 17:54:33.

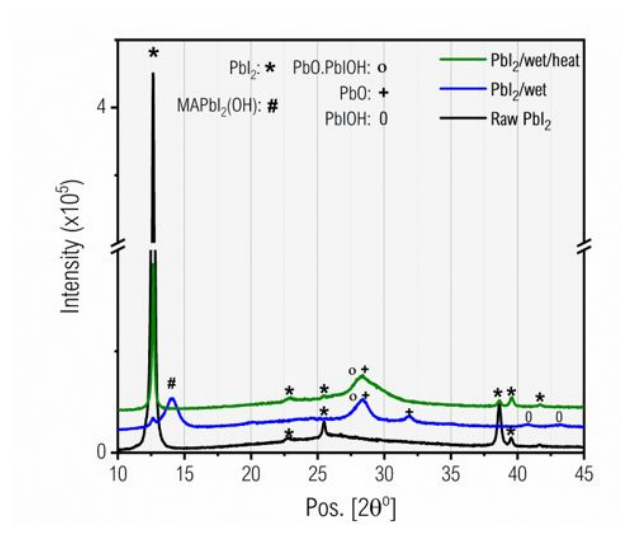


Figure 5: XRD patterns of Raw-Pbl₂, Pbl₂/wet and Pbl₂/wet/heat films

MAPbl₂OH pseudo-perovskite⁵¹. Other additional peaks of Pbl₂/wet at 28.39°, 31.87°, 40.80°, and 43.26° are associated with lead oxide and hydroxide compounds, specifically PbO.PbIOH, PbO, and PbIOH. Upon heating (PbI₂/wet/heat),

peak at 14.11° disappears, whereas the peak at corresponding DOI: 10.1039/D5EL00143A to PbO.PbIOH (28.2°) persists.

XPS survey spectra of investigated PbI₂ films is shown in Figure S5. Similarly, C 1s, O 1s, Pb 4f and I 3d orbitals are clearly identified, in which Pb 4f elemental spectra are deconvoluted for discussion. As shown in Figure 6a, Raw-Pbl2 exhibits a dominant peak at 138.9 eV, attributed to the Pb-I in PbI₂, along with a minor peak at 137.1 eV (shown in Figure S6), corresponding to Pb-O in the PbI2(DMSO)x complex, respectively⁵²⁻⁵⁴. For Pbl₂/wet (Figure 6b), a shift in binding energy to 138.76 eV is observed, enabling the fitting of an additional peak at 138.7 eV, which corresponds to Pb-OH bonding. Upon heating (Pbl2/wet/heat), the removal of MAOH reduces the Pb-OH contribution, causing the main peak to revert to 138.84 eV (Figure 6c). Figure 6d summarizes the bonding ratio of lead species in the PbI₂ film, which is normalized by the area of Pb 4f_{7/2} peak. In the Raw-Pbl₂ films, the Pb-I bonds dominate, accounting for 96.3%, with a small fraction of Pb-O bonds as 3.7%. In contrast, the Pbl2/wet film shows a dramatic decrease in Pb-I bonding to 53.4%, accompanied by a significant increase in Pb-OH bonding to 40%, and a slight rise in Pb-O bonding to 6.6%, indicating the

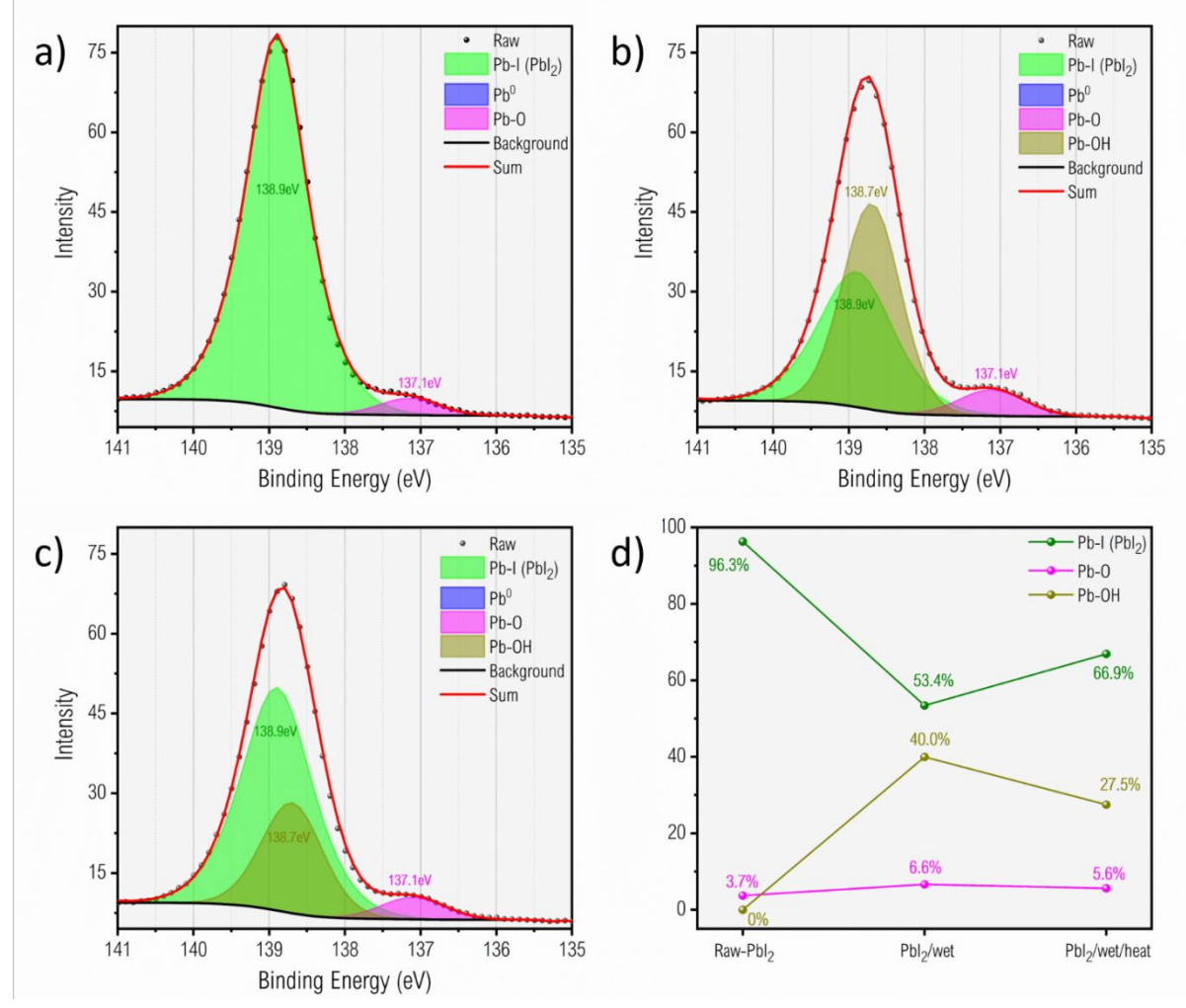


Figure 6: a, b, c) XPS Pb 4f_{7/2} regions and d) binding ratios of Raw-Pbl₂, Pbl₂/wet, Pbl₂/wet/heat films

Open Access Article. Published on 04 nóvember 2025. Downloaded on 14.11.2025 17:54:33.

ARTICLE EES Solar

formation of lead hydroxide and lead oxide in the Pbl₂/wet film. Upon annealing (the Pbl₂/wet/heat), the Pb–I bond ratio increases moderately to 66.9%, while Pb–OH and Pb–O decrease modestly to 27.5% and 5.6%, respectively. These results indicate that the interaction of Pbl₂ film and MA⁰ under humid conditions leads to the formation of Pb–OH and Pb–O, both will remain in the resultant film, even with a post-heating treatment.

Similarly, possible reactions involved in MATM on PbI₂ film in the presence of moisture are proposed below. Ideally, PbI₂ chemisorbs MA⁰ to form a liquid-phase PbI₂ $\cdot x$ MA⁰ complex:

$$\chi MA_{(gas)}^{0} + PbI_{2(solid)} \rightarrow PbI_{2} \cdot \chi MA_{(liquid)}^{0}$$
(8)

However, water can also react with MA 0 , as mentioned previously in reaction (2). Or with adsorbed MA 0 intermediate, eventually forming PbI $_2 \cdot x$ MAOH:

$$PbI_2 \cdot xMA_{(liquid)}^0 + H_2O_{(gas)} \rightarrow PbI_2 \cdot xMAOH_{(liquid)}$$
 (9)

The OH $^-$ can exchange with I $^-$ to produce pseudo perovskite MAPbI $_2$ OH and PbI $_2 \cdot$ MAOH intermediate:

$$PbI_2 \cdot xMAOH_{(liquid)} \rightarrow yMAPbI_2OH_{(solid)} + (1-y)PbI_2 \cdot (x-y)MAOH_{(liquid)}$$
 (10)

The pseudo perovskite and intermediate can Artifurther decompose into PbIOH and PbO:

DOI: 10.1039/D5EL00143A

$$PbI_{2} \cdot (x - y)MAO^{H}(liquid) \rightarrow$$

$$PbI_{2}(solid) + (x - y)MAO^{H}(gas)$$
(11)

$$MAPbI_2OH_{(solid)} \rightarrow MAI_{(solid)} + PbIOH_{(solid)}$$
 (12)

PbIOH further decomposes into PbO and H_2O as mentioned above in reaction (7).

Morphology analysis

Figure 7 illustrates the SEM and AFM topographies of the investigated MAPbI₃ films. Primary-MAPbI₃ film (Figure 7a), consists of large MAPbI₃ grains ranging from 500 to 2000 nm, rendering to a rough surface with a surface roughness (Sa) of 66.7 nm. All MA⁰-treated samples reveal significantly reduced surface roughness. Sa of 2nd-MAPbI₃/dry, 2nd-MAPbI₃/wet and 2nd-MAPbI₃/wet/heat are 13.96 nm, 12.58 nm and 14.16 nm, respectively. Due to the inherent dissolution–recrystallization behaviour of MATM, the significant reduction in Sa values observed in the three MATM-treated samples is expected, as this mechanism naturally smoothens the MAPbI₃ film surface. The top-view images of 2nd-MAPbI₃/dry (Figure 7b) and 2nd-MAPbI₃/wet (Figure 7c) show almost no discernible differences, either in SEM morphology or Sa values.

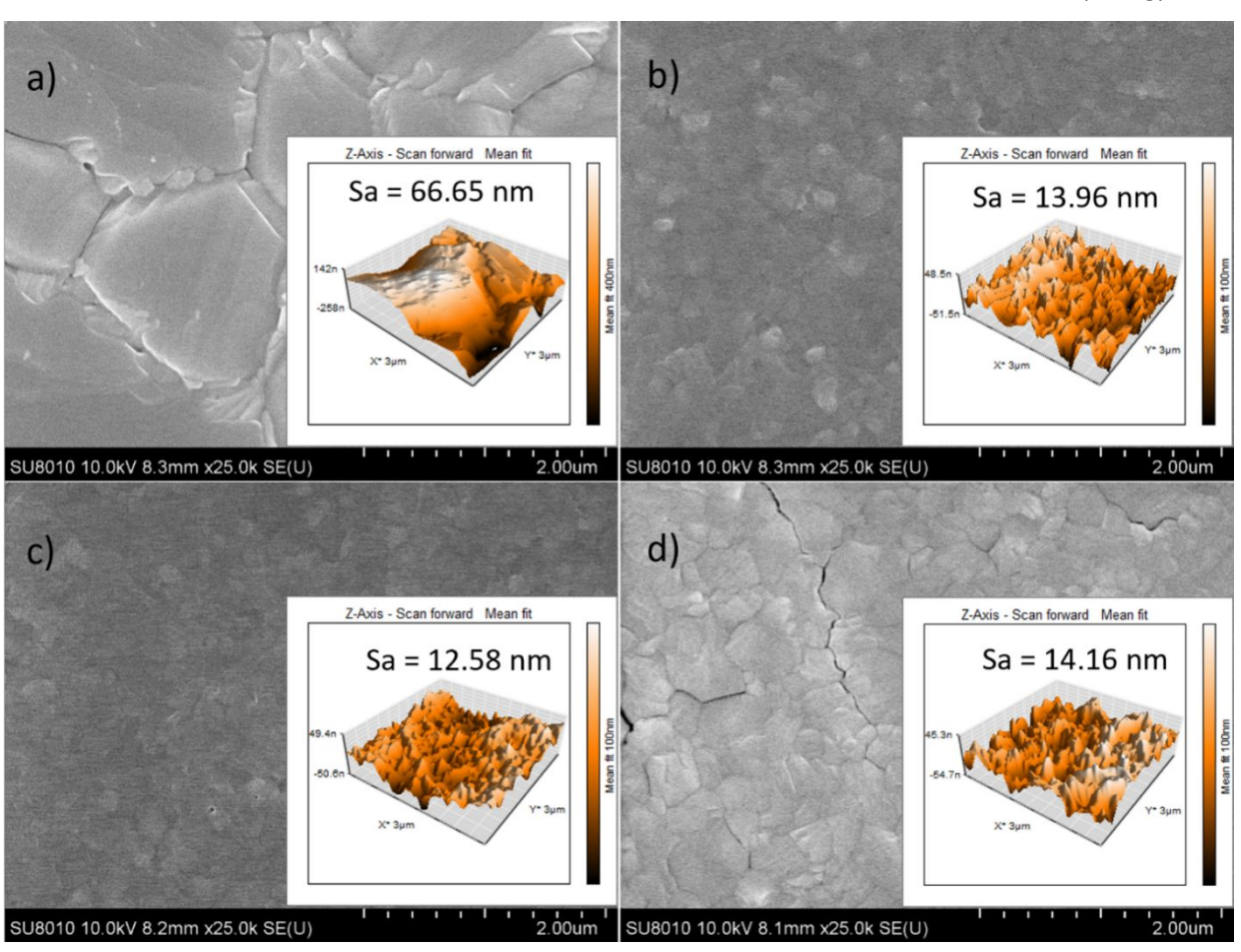


Figure 7: SEM topographic view and AFM of PVSK films: a) Primary-MAPbl₃, b) 2nd-MAPbl₃/dry, c) 2nd-MAPbl₃/wet and d) 2nd-MAPbl₃/wet/heat films

EES Solar ARTICLE

fact, this is not favourable for the practical operation of MATM, as the chemical composition of 2nd-MAPbl₃/wet has already deteriorated, as discussed above. Its seemingly smooth and uniform surface morphology may lead to a misleading assessment of film quality. On the other hand, a closer inspection of the 2nd-MAPbI₃/wet/heat sample (Figure 7d) reveals the presence of prominent cracks, indicating that the moisture content during MATM may still affect the integrity of the resultant film. Based on the preceding discussion, we have reason to believe that the outgassing of MAOH during the postheating process of the 2nd-MAPbI₃/wet sample is the primary cause of the observed cracking.

Optoelectrical properties

This article is licensed under a Creative Commons Attribution 3.0 Unported Licence.

Open Access Article. Published on 04 nóvember 2025. Downloaded on 14.11.2025 17:54:33.

Figure 8a presents the UV-vis absorption spectra of Primary-MAPbl₃ and 2nd-MAPbl₃ films. The three 2nd-MAPbl₃ films exhibit similar absorbance in the 650-900 nm range, whereas the Primary-MAPbl₃ film demonstrates a higher overall absorbance. The reduced absorbance observed in the 2nd-MAPbl₃ films is attributed to their lower surface roughness (Sa),

which reduces light scattering. The Tauc-plot derived from the absorption spectra, shown in Figure 86, indicates that the optical bandgap (Eg) of the Primary-MAPbI₃ film is 1.591 eV. In contrast, the **2nd-MAPbl**₃ films exhibit a slightly higher E_a of approximately 1.600 eV. The change is small and is likely due to the preferred (110) crystallographic orientation in the MAPbI₃ PVSK structure^{24, 31}.

Space-charge-limited current (SCLC) measurements were conducted to quantitatively assess the impact on trap-filling limited voltage (V_{TFL}) and trap density (N_t). The corresponding SCLC curves are presented in Figure 8c. The V_{TFL} value is identified at the transition point between the Ohmic and trapfilled limit (TFL) regions, while Nt is determined using the following equation:

$$Nt = 2\varepsilon\varepsilon_o \frac{V_{TFL}}{eL^2}$$

In this equation, e represents the elementary charge (1.602 × 10^{-19} C), ε_0 denotes the vacuum permittivity (8.854 × 10^{-12} F/m), ε corresponds to the relative dielectric constant of MAPbI₃ (32),

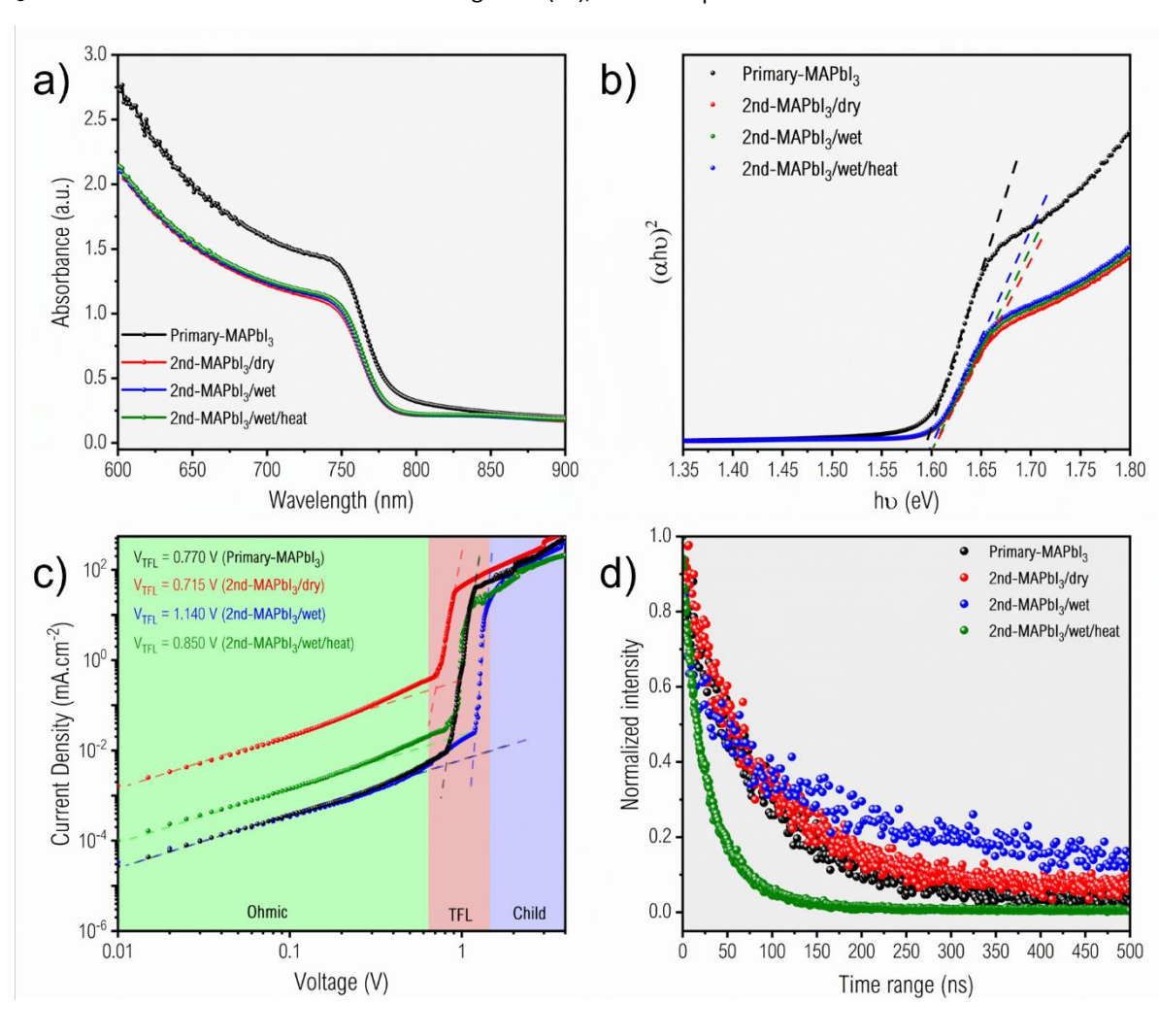


Figure 8: a) UV-vis absorption spectra, b) Tauc-plot, c) the SCLC curves and d) the TRPL spectra of Glass/Al₂O₃/PVSK film of Primary-MAPbI₃, 2nd-MAPbI₃/dry, 2nd-MAPbI₃/wet and 2nd-MAPbI₃/wet/heat films

ven Access Article. Published on 04 nóvember 2025. Downloaded on 14.11.2025 17:54:33.

ARTICLE

EES Solar

Table 1: Optoelectronic parameters of various MAPbl₃ films

View Article Online DOI: 10.1039/D5EL00143A

	Primary-MAPbI₃	2nd-MAPbl₃/dry	2nd-MAPbl₃/wet	2nd-MAPbl₃/wet /heat
$V_{TFL}(V)$	0.770	0.715	1.14	0.850
N _t (x10 ¹⁶ cm ⁻³)	1.421	1.250	1.993	1.486
$ au_1$ (ns)	8.69	31.08	3.55	12.15
A1 (%)	11.19	26.05	43.33	36.52
$ au_2$ (ns)	93.19	108.46	120.71	39.23
A2 (%)	88.81	73.95	56.67	63.48
$ au_{\sf avg}$ (ns)	83.74	88.30	69.95	29.34

and L signifies the thickness of the perovskite film. A summary of the V_{TFL} and N_t values for the examined samples is provided in Table 1. The Primary-MAPbI₃ exhibits a V_{TFL} of 0.770 V and a N_t of 1.42×10^{16} cm⁻³. **2nd-MAPbI₃/dry** demonstrates a reduced V_{TFL} (0.715 V) and N_t (1.25 × 10¹⁶ cm⁻³), suggesting that the quality of the film is enhanced by the MATM process, which is consistent with previous studies31. However, at 2nd-MAPbl₃/wet, both V_{TFL} and N_t exhibit a significant increase, reaching 1.14 V and 1.99×10^{16} cm⁻³, respectively. This indicates that impurities such as MAPbI₂OH, PbO, and PbIOH introduce a higher density of defect-trap states within the crystal lattice. Following post-heating treatment (2nd-MAPbl₃/wet/heat), a substantial portion of MAOH is removed; however, residual PbO and PbIOH persist in the perovskite film, contributing to an elevated defect density, measured at 1.486×10^{16} cm⁻³.

The carrier lifetime of the investigated samples was probed using time-resolved photoluminescence (TRPL). The TRPL data shown in Figure 8d were fitted with the following bi-exponential function:

$$I(t) = A_1 e^{-\frac{t}{\tau_1}} + A_2 e^{-\frac{t}{\tau_2}} + I_0$$

where A₁ and A₂ represent the pre-exponential factors, while I₀ is a constant accounting for the background signal. The short lifetime (τ_1) is primarily associated with non-radiative surface recombination, whereas the long lifetime (τ_2) corresponds to bulk radiative recombination within the PVSK film.

We subsequently calculated the average carrier lifetime using the amplitude-weighted method⁵⁵:

$$\tau_{avg} = \frac{\sum (A_i \tau_i)}{\sum (A_i)}$$

The results are summarized in Table 1. The Primary-MAPbI₃ film shows a τ_1 of 8.69 ns and a τ_2 of 93.19 ns, with an average lifetime (τ_{avg}) of 83.74 ns. For the **2nd-MAPbl₃/dry** sample, both τ_1 , τ_2 and τ_{avg} increase to 31.08 ns, 108.46 ns, and 88.30 ns, respectively, indicating that when the MATM process proceeds without moisture interference, both film integrity and trap density are improved.

For the moisture-affected samples (2nd-MAPbI₃/wet and 2nd-MAPbl₃/wet/heat), a shorter τ_{avg} is observed, suggesting that the moisture-induced photovoltaic-inactive hydrated byproducts adversely influence carrier lifetime and consequently degrade photovoltaic properties. Interestingly, the 2nd-MAPbl₃/wet film exhibits the longest τ_2 (120.71 ns) but simultaneously the shortest τ_1 (3.55 ns) among all samples. We attribute this phenomenon to moisture-induced, photovoltaic-inactive phases forming electrically isolated high-quality domains, which artificially inflate the average PL lifetime - resulting in a pseudo-long lifetime - while the majority of photogenerated carriers still undergo rapid non-radiative interfacial recombination before reaching the charge-transport layers, as evidenced by the shortest τ_1 . Combining TRPL and SCLC analysis, it is evident that the existence of impurities such as MAPbl₂OH, PbO, and PbIOH formed during moisture-involved MATM lead to the reduction in electron lifetime. As for 2nd-MAPbI₃/wet/heat, both τ_1 and τ_2 became shorter even compared with Primary-MAPbl3, saying that even with a post-heating treatment, the damage of MAPbI₃ due to improper MATM is difficultly reverted. We attribute this is because although post-heating removes certain OH-species, the post-heating itself also induces fast diffusion of impurities from surface to bulk film. Such effect increases trap density and eventually shortens the electron lifetime of the entire PVSK film.

Photovoltaic performance

Table 2 and Figure S7 illustrates the photovoltaic statistics of the PSC made with the investigated MAPbI₃ films. J-V curves of the best-performing devices is plotted in Figure 9a, in which the best Primary-MAPbl₃-based device exhibited a PCE of 16.55%, with a short-circuit current density (J_{SC}) of 21.41 mA/cm², an open-circuit voltage (Voc) of 1.01 V, and a fill factor (FF) of 76.30%. For 2nd-MAPbl₃/dry-based devices, improved PVSK film quality led to an increase in all photovoltaic parameters. The best-performing PSC employed with 2nd-MAPbl₃/dry showed J_{SC}, V_{OC}, and FF of 23.78 mA/cm², 1.04 V, and 78.71%, respectively, resulting in an improved PCE of 19.48%. If the MATM underwent with moisture interference, PCEs of the devices declined considerably to 16.11% and 18.74%, for the 2nd-MAPbl₃/wet and 2nd-MAPbl₃/wet/heat, respectively. This result once again highlights the critical importance of environmental conditions during MATM of

Open Access Article. Published on 04 nóvember 2025. Downloaded on 14.11.2025 17:54:33.

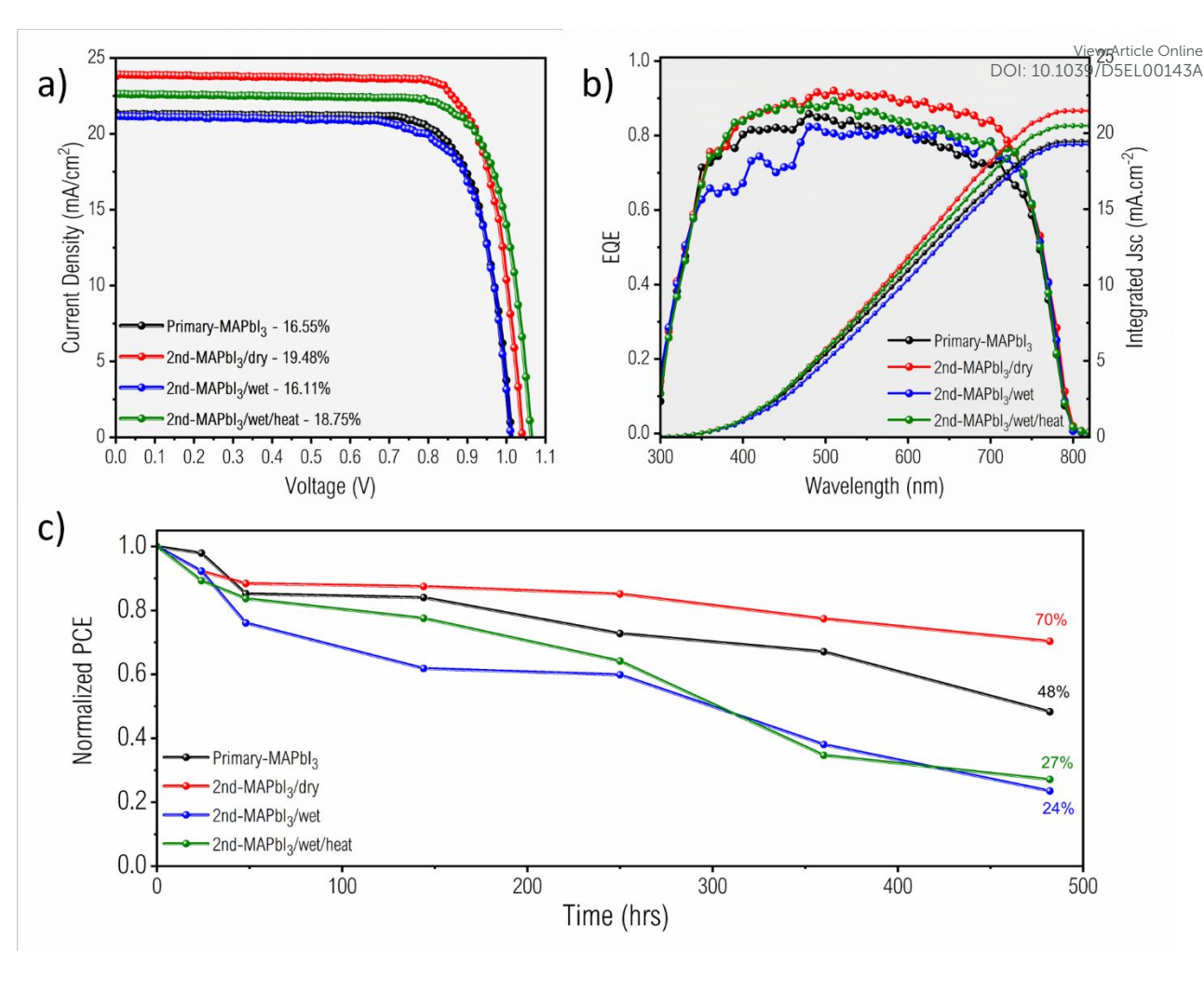


Figure 9: a) The best performance J-V curves of perovskite MAPbI₃ devices with Primary-MAPbI₃ and 2nd-MAPbI₃ (backward scan); b) EQE and integrated J_{SC} of perovskite MAPbl₃ devices and c) Stability of devices made from Primary-MAPbI₃ and 2nd-MAPbI₃ films

Table 2: Photovoltaic parameters of various MAPbl₃ films (based on 15 Cells)

Device	EQE-J _{SC} (mA/cm²)		J _{SC} (mA/cm²)	V _{oc} (V)	FF (%)	PCE (%)	ні
	19.47	Champion	21.41	1.01	76.30	16.55	0.30
Primary-MAPbI₃		Average	22.36 ± 0.68	0.99 ± 0.02	72.03 ± 3.55	15.91 ± 0.63	
	21.50	Champion	23.78	1.04	78.71	19.48	0.07
2nd-MAPbl₃/dry		Average	22.97 ± 0.55	1.04 ± 0.02	77.63 ± 1.52	18.67 ± 0.56	
	19.28	Champion	21.19	1.01	75.81	16.11	0.09
2nd-MAPbl₃/wet		Average	20.98 ± 0.86	1.00 ± 0.01	67.04 ± 4.43	14.10 ± 0.79	
and 2.2.21. / . // .	neat 20.50	Champion	22.64	1.06	77.86	18.74	0.08
2 nd -MAPbl ₃ /wet/heat		Average	22.49 ± 0.31	1.05 ± 0.02	73.27 ± 2.74	17.26 ± 0.80	

MAPbl₃ films. In particular, in the presence of moisture, although surface morphology can still be effectively smoothened, the formation of undesirable by-products significantly deteriorates the optoelectronic properties of the resultant MAPbI₃ films, ultimately leading to decreased device performance rather than improvement.

The hysteresis index (HI), which is defined as:

en Access Article. Published on 04 nóvember 2025. Downloaded on 14.11.2025 17:54:33.

EES Solar

ARTICLE

$$HI = \frac{\left(PCE_{reverse\ scan} - PCE_{forward\ scan}\right)}{PCE_{reverse\ scan}}$$

is a key indicator for evaluating trap-assisted recombination, surface charge recombination, and ion migration in PSCs. As can be seen in Figure S8 and Table S1, Primary-MAPbI₃ exhibited a relatively large HI of 0.30, confirming its significant hysteresis behavior. In contrast, all three types of 2nd-MAPbI₃ devices demonstrated substantially reduced HI values (0.07-0.09), highlighting that the liquefaction-recrystallization mechanism of MATM effectively improves film uniformity and compactness, leading to suppressed hysteresis. Among the three 2nd-MAPbI₃ devices, the 2nd-MAPbI₃/dry film showed the lowest HI compared to the 2nd-MAPbI₃/wet and 2nd-MAPbl₃/wet/heat films. This increase in hysteresis for the latter two devices is primarily attributed to the presence of photovoltaic-inactive impurities introduced by moisture during MATM, which results in higher defect density within the perovskite film.

Overall, based on the current results, improved film compactness appears to be the dominant factor in hysteresis suppression, which is a fundamental benefit provided by the MATM process. With further refinement of MATM operation—particularly by eliminating moisture interference—the enhancement in film quality and corresponding hysteresis reduction can be further strengthened.

Figure 9b shows the incident photon-to-electron conversion efficiency (IPCE) spectra of the four investigated devices. The integrated J_{SC} values are 19.47 mA/cm² for **Primary-MAPbI₃**, 21.50 mA/cm² for **2nd-MAPbI₃/dry**, 19.28 mA/cm² for **2nd-MAPbI₃/wet**, and 20.50 mA/cm² for **2nd-MAPbI₃/wet/heat**, which are consistent with the trend observed in the J–V characteristics.

For **2nd-MAPbl₃/wet** device, the reduced integrated J_{SC} can be attributed to two major factors. First, the EQE is significantly suppressed in the 300–450 nm region, suggesting enhanced surface recombination or parasitic absorption at the transport-layer/perovskite interface (e.g., $TiO_2/PVSK$)⁵⁶. This is supported by the shortened TRPL lifetime ($\tau_1 \approx 3.55$ ns) and pronounced SSPL quenching in the 2nd-MAPbl₃/wet films. A slight suppression in this region is also found for **Primary-MAPbl**₃, indicating the presence of residual surface recombination. Second, the suppressed EQE in the 500–750 nm region indicates an increase in bulk recombination due to the presence of intrinsic defects in the perovskite film. This interpretation is further validated by the results from SSPL, SCLC, and TRPL characterizations.

Overall, MATM performed under dry conditions effectively improves perovskite film morphology, heals defects, and reduces trap density, thereby contributing to the enhancement of photovoltaic performance.

Notably, although the **2nd-MAPbl3** films exhibit a reduced average grain size compared with the **Primary-MAPbl3** films, their device performance is significantly improved. This observation contrasts with the widely accepted understanding that larger perovskite grains are beneficial for reducing defect density and enhancing optoelectronic properties. Such a counter-intuitive result highlights

that grain size is not the sole dominant factor determining device performance. Instead, the MATM improves existing applie quality, film compactness and suppressed defect formation through a liquefaction—recrystallization mechanism. These improvements collectively facilitate enhanced charge extraction and reduced non-radiative recombination losses, ultimately leading to superior photovoltaic performance despite the smaller grain size. Our results therefore reinforce that structural coherence, defect passivation, and film continuity can outweigh grain-size effects in governing PSC efficiency.

To evaluate the impact of moisture during MATM on the stability of PSC, we fabricated both Primary-MAPbI₃ and 2nd-MAPbl₃ films, storing them under controlled humidity conditions (15-25%) without encapsulation. As shown in Figure 9c, the long-term stability of PSCs fabricated from Primary-MAPbl₃, 2nd-MAPbl₃/dry, 2nd-MAPbl₃/wet, and 2nd-MAPbl₃-MAPbl₃/wet/heat was systematically compared. After more than 480 hours of ambient storage, PSCs based on 2nd-MAPbl₃/dry films retained 70% of their initial power conversion efficiency (PCE), while devices based on Primary-MAPbl₃ retained only 48%. In contrast, devices that underwent MA⁰ treatment in the presence of moisture and those subjected to heating exhibited markedly degradation, retaining only 24% and 27% of their initial PCE, respectively.

These results indicate that the incorporation of impurities during the moisture-influenced MATM process significantly accelerates device degradation. Furthermore, the MATM process conducted within the MALCR system, which functions as a moisture-isolated environment, yields enhanced device stability compared to PSCs fabricated using untreated **Primary-MAPbI**₃ films.

Upscaling PSC using moisture-free MATM

After confirming that proper implementation of MATM can simultaneously enhance both the efficiency and stability of PSCs, we further investigated another critical advantage of this technique: its applicability in the fabrication of large-area perovskite solar modules. In addition to the laboratory-scale small-area devices (0.056 cm²), we progressively scaled up the active area to $8.15~\text{cm}^2$ (a $4.0~\text{cm} \times 4.0~\text{cm}$ module consisting of six sub-cells in series) and $16.24~\text{cm}^2$ (a $5.0~\text{cm} \times 5.0~\text{cm}$ module comprising seven sub-cells in series).

Figure 10 and Table 3 summarize the performance statistics of PSCs with various active areas. Remarkably, under identical device architecture, material composition, and processing conditions, the PCE remained essentially unchanged across different device scales. The laboratory-scale small-area cell exhibited a PCE of 19.68%, while the 8.15 cm² and 16.24 cm² modules achieved PCEs of 19.60% and 19.57%, respectively. This demonstrates a truly lossless scaling process and represents a significant milestone in the upscaling of high-performance PSC modules.

FFS Solar ARTICIF

Table 3: Photovoltaic parameters of 2nd-MAPbI₃/dry devices at different active area (based on 5 devices) Article Online DOI: 10.1039/D5EL00143A

PSC		J _{SC} (mA/cm ²)	V _{oc} (V)	FF (%)	PCE (%)
Cell with	Champion	23.78	1.04	78.71	19.48
active area of 0.056 cm ²	Average	23.43 ± 0.38	1.04 ± 0.02	78.57 ± 1.05	19.25 ± 0.21
Module with	Champion	3.85	6.73	75.66	19.60
active area of 8.15 cm ²	Average	3.81 ± 0.11	6.69 ± 0.09	74.77 ± 1.48	19.06 ± 0.50
Module with	Champion	3.23	7.87	77.00	19.57
active area of 16.24 cm ²	Average	3.22 ± 0.06	7.47 ± 0.30	78.78 ± 1.61	18.93 ± 0.66

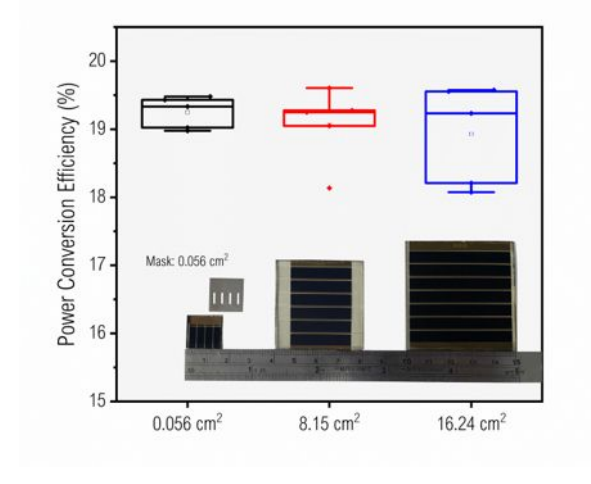


Figure 10: Performance of small devices and module devices

Conclusions

This article is licensed under a Creative Commons Attribution 3.0 Unported Licence.

Then Access Article. Published on 04 nóvember 2025. Downloaded on 14.11.2025 17:54:33.

study systematically elucidates the environmental moisture on the MATM of MA-based perovskite films and its implications for scalable PSC manufacturing. We demonstrate that uncontrolled humidity during MATM induces the formation of photoinactive by-products such as PbO, PbIOH, and MAPbl₂OH, which significantly deteriorate the film's crystallinity, increase trap-state density, and shorten carrier lifetimes. More importantly, the formation of these by-products is uncontrollable, which significantly undermines the feasibility and yield of large-area MATM processing. These defects not only compromise photovoltaic performance but also severely accelerate device degradation. In contrast, performing MATM in a dry condition effectively preserves the liquefactionrecrystallization benefits while preventing deleterious side reactions. Devices treated under dry conditions exhibit superior PCE of 19.48% and improved long-term stability from a control device with an initial 16.67% PCE. We further demonstrated the scalability of the moisture-free MATM protocol by successfully increasing the device area from 0.056 cm² to 16.24 cm² without statistical loss in PCE. This clearly highlights the tremendous potential of properly implemented MATM for the fabrication of large-area perovskite films.

Author contributions

Tzu-Chien Wei supervised the study. Duc-Anh Le conceived the idea, designed the experiments, and wrote the first manuscript draft. Both authors contributed to the writing and revision.

Conflicts of interest

There are no conflicts to declare.

Data availability

The data supporting this article have been included as part of the ESI. † More raw data are available from the corresponding author on reasonable request.

Acknowledgements

This project has received funding from the National Science and Technology Council (114-2811-E-007-021) and a grant from National Tsing-Hua University (113Q2750E1).

Notes and references

- J. S. Manser and P. V. Kamat, Nature Photonics, 2014, 8,
- 2. S. De Wolf, J. Holovsky, S.-J. Moon, P. Löper, B. Niesen, M. Ledinsky, F.-J. Haug, J.-H. Yum and C. Ballif, The Journal of Physical Chemistry Letters, 2014, 5, 1035-1039.
- 3. S. D. Stranks, G. E. Eperon, G. Grancini, C. Menelaou, M. J. P. Alcocer, T. Leijtens, L. M. Herz, A. Petrozza and H. J. Snaith, Science, 2013, 342, 341-344.
- G. Xing, N. Mathews, S. Sun, S. S. Lim, Y. M. Lam, M. 4. Grätzel, S. Mhaisalkar and T. C. Sum, Science, 2013, 342,
- 5. G. E. Eperon, S. D. Stranks, C. Menelaou, M. B. Johnston, L. M. Herz and H. J. Snaith, Energy & Environmental Science, 2014, 7, 982-988.
- The National Renewable Energy Laboratory, https://www.nrel.gov/pv/cell-efficiency.html.
- 7 A. Kojima, K. Teshima, Y. Shirai and T. Miyasaka, Journal of the American Chemical Society, 2009, 131, 6050-6051.
- M. Saliba, J.-P. Correa-Baena, C. M. Wolff, M. Stolterfoht, 8. N. Phung, S. Albrecht, D. Neher and A. Abate, Chemistry of Materials, 2018, 30, 4193-4201.
- 9. Y. Galagan, F. Di Giacomo, H. Gorter, G. Kirchner, I. de Vries, R. Andriessen and P. Groen, Advanced Energy Materials, 2018, 8, 1801935.

Open Access Article. Published on 04 nóvember 2025. Downloaded on 14.11.2025 17:54:33.

ARTICLE EES Solar

- A. T. Barrows, A. J. Pearson, C. K. Kwak, A. D. F. Dunbar, A. R. Buckley and D. G. Lidzey, Energy & Environmental Science, 2014, 7, 2944-2950.
- H. Cai, X. Liang, X. Ye, J. Su, J. Guan, J. Yang, Y. Liu, X. Zhou, R. Han, J. Ni, J. Li and J. Zhang, ACS Applied Energy Materials, 2020, 3, 9696-9702.
- 12. Q. Yao, Z. Gu, C. Chen, Y. Jiang, Z. Su, J. Wang, T. Niu, T. Pan, Y. Xia, L. Zheng, X. Gao, J. Zhang, X. Duan, L. Chao and Y. Chen, Angewandte Chemie International Edition, 2025, 64, e202501350.
- 13. H. Eggers, F. Schackmar, T. Abzieher, Q. Sun, U. Lemmer, Y. Vaynzof, B. S. Richards, G. Hernandez-Sosa and U. W. Paetzold, Advanced Energy Materials, 2020, 10, 1903184.
- 14. H. Wang, W. Zeng and R. Xia, Thin Solid Films, 2018, 663, 9-13.
- 15. A. D. Taylor, Q. Sun, K. P. Goetz, Q. An, T. Schramm, Y. Hofstetter, M. Litterst, F. Paulus and Y. Vaynzof, Nature Communications, 2021, 12, 1878.
- 16. P. Chen, X. Ma, Z. Wang, N. Yang, J. Luo, K. Chen, P. Liu, W. Xie and Q. Hu, Physical Chemistry Chemical Physics, 2024, 26, 14874-14882.
- 17. Q. Chen, H. Zhou, Z. Hong, S. Luo, H.-S. Duan, H.-H. Wang, Y. Liu, G. Li and Y. Yang, Journal of the American Chemical Society, 2014, **136**, 622-625.
- 18. S. Zhang, Y. Ge, X. Qin, X. Wang, T. Tao, L. Yu, X. Song, Y. Jiang and C. Xia, Advanced Functional Materials, 2025, 35, 2418968.
- 19. Z. Su, Y. Sun, B. Yu and H. Yu, ACS Applied Materials & Interfaces, 2024, 16, 43489-43497.
- 20. A. Perveen, Y. Xu, S. M. Abubakar, P. Sellan, W. Xin, F. Saeed, S. Hussain, B. S. Bae, J. Zhou, Y. Zhu and W. Lei, Advanced Optical Materials, 2024, 12, 2302918.
- 21. Z. Xiao, Q. Dong, C. Bi, Y. Shao, Y. Yuan and J. Huang, Advanced Materials, 2014, 26, 6503-6509.
- 22. Y. Tu, J. Wu, X. He, P. Guo, T. Wu, H. Luo, Q. Liu, K. Wang, J. Lin, M. Huang, Y. Huang, Z. Lan and S. Li, Journal of Materials Chemistry A, 2017, 5, 4376-4383.
- 23. M. Chen, Z. Qin, Z. Zhang, Y. Wang and L. Han, Energy & Environmental Science, 2025, 18, 5952-5960.
- 24. Y. Chang, L. Wang, J. Zhang, Z. Zhou, C. Li, B. Chen, L. Etgar, G. Cui and S. Pang, Journal of Materials Chemistry A, 2017, 5, 4803-4808.
- 25. Z. Zhou, Z. Wang, Y. Zhou, S. Pang, D. Wang, H. Xu, Z. Liu, N. P. Padture and G. Cui, Angewandte Chemie International Edition, 2015, 54, 9705-9709.
- 26. B. Ding, Y. Ding, J. Peng, J. Romano-deGea, L. E. K. Frederiksen, H. Kanda, O. A. Syzgantseva, M. A. Syzgantseva, J.-N. Audinot, J. Bour, S. Zhang, T. Wirtz, Z. Fei, P. Dörflinger, N. Shibayama, Y. Niu, S. Hu, S. Zhang, F. F. Tirani, Y. Liu, G.-J. Yang, K. Brooks, L. Hu, S. Kinge, V. Dyakonov, X. Zhang, S. Dai, P. J. Dyson and M. K. Nazeeruddin, *Nature*, 2024, **628**, 299-305.
- 27. Y. Deng, C. H. Van Brackle, X. Dai, J. Zhao, B. Chen and J. Huang, Science Advances, 2020, 5, eaax7537.
- 28. J. Li, J. Dagar, O. Shargaieva, O. Maus, M. Remec, Q. Emery, M. Khenkin, C. Ulbrich, F. Akhundova, J. A. Márquez, T. Unold, M. Fenske, C. Schultz, B. Stegemann, A. Al-Ashouri, S. Albrecht, A. T. Esteves, L. Korte, H. Köbler, A. Abate, D. M. Többens, I. Zizak, E. J. W. List-Kratochvil, R. Schlatmann and E. Unger, Advanced Energy Materials, 2023, 13, 2203898.

- R. Zhao, L. Tan, X. Luo, J. He, R. Dai, C. Feng, Q. Zhang Jaine 29. Yang and Y. Chen, Angewandte Chemie International 0143A Edition, 2024, 63, e202319100.
- 30. M.-J. Zhang, N. Wang, S.-P. Pang, Q. Lv, C.-S. Huang, Z.-M. Zhou and F.-X. Ji, ACS Applied Materials & Interfaces, 2016, 8, 31413-31418.
- D.-A. Le, K. Kala, T.-S. Su, N. Perumbalathodi and T.-C. 31. Wei, Solar RRL, 2024, 8, 2400553.
- 32. T. Zhao, S. T. Williams, C.-C. Chueh, D. W. deQuilettes, P.-W. Liang, D. S. Ginger and A. K. Y. Jen, RSC Advances, 2016, 6, 27475-27484.
- H. Fan, J.-H. Huang, L. Chen, Y. Zhang, Y. Wang, C. Gao, P. 33. Wang, X. Zhou, K.-J. Jiang and Y. Song, Journal of Materials Chemistry A, 2021, 9, 7625-7630.
- 34. J.-a. Yang, T. Qin, L. Xie, K. Liao, T. Li and F. Hao, Journal of Materials Chemistry C, 2019, 7, 10724-10742.
- Y. Jiang, E. J. Juarez-Perez, Q. Ge, S. Wang, M. R. Leyden, 35. L. K. Ono, S. R. Raga, J. Hu and Y. Qi, Materials Horizons, 2016, 3, 548-555.
- Z. Xu, N. Liu, X. Liu, W. Han, W. Xu, J. Zhang, L. Huang, Z. 36. Hu and Y. Zhu, Chemical Engineering Journal, 2023, 451, 139047.
- 37. G. I. Gurina and K. V. Savchenko, Journal of Photochemistry and Photobiology A: Chemistry, 1995, 86, 81-84.
- 38. R. A. Kerner, T. H. Schloemer, P. Schulz, J. J. Berry, J. Schwartz, A. Sellinger and B. P. Rand, Journal of Materials Chemistry C, 2019, 7, 5251-5259.
- 39. D. Bogachuk, L. Wagner, S. Mastroianni, M. Daub, H. Hillebrecht and A. Hinsch, Journal of Materials Chemistry A, 2020, 8, 9788-9796.
- 40. L. Gao, X. Li, Y. Liu, J. Fang, S. Huang, I. Spanopoulos, X. Li, Y. Wang, L. Chen, G. Yang and M. G. Kanatzidis, ACS Applied Materials & Interfaces, 2020, 12, 43885-43891.
- 41. O. I. Siidra, D. Y. Zenko, A. N. Suknotova and S. V. Krivovichev, Mineralogical Magazine, 2013, 77, 3239-3248.
- 42. P. Boher, P. Garnier, J. R. Gavarri and A. W. Hewat, Journal of Solid State Chemistry, 1985, 57, 343-350.
- 43. R. W. G. Wyckoff, Crystal Structures, Interscience Publishers, New York, 2nd edn., 1963.
- 44. R. Guo, B. Dahal, A. Thapa, Y. R. Poudel, Y. Liu and W. Li, Nanoscale Advances, 2021, 3, 2056-2064.
- 45. M. Bruggeman, M. Zelzer, H. Dong and A. Stamboulis, Surface and Interface Analysis, 2022, 54, 986-1007.
- 46. A. Babayigit, D. Duy Thanh, A. Ethirajan, J. Manca, M. Muller, H.-G. Boyen and B. Conings, Scientific Reports, 2016, 6, 18721.
- 47. N. Ahn, K. Kwak, M. S. Jang, H. Yoon, B. Y. Lee, J.-K. Lee, P. V. Pikhitsa, J. Byun and M. Choi, Nature Communications, 2016, **7**, 13422.
- 48. T.-S. Su, T.-E. Fan, H.-K. Si, D.-A. Le, N. Perumbalathodi and T.-C. Wei, Solar RRL, 2021, 5, 2100109.
- 49. X. Zhang, J. Ye, L. Zhu, H. Zheng, G. Liu, X. Liu, B. Duan, X. Pan and S. Dai, Nanoscale, 2017, 9, 4691-4699.
- Z. Yang, X. Cao, G. Niu, Y. Wang, Y. Dong, S. Cao, W. Liu, X. 50. Wang, Y. Liu and J. Wang, Chemical Engineering Journal, 2023, 464, 142720.
- M. Long, T. Zhang, H. Zhu, G. Li, F. Wang, W. Guo, Y. Chai, 51. W. Chen, Q. Li, K. S. Wong, J. Xu and K. Yan, Nano Energy, 2017, 33, 485-496.

View Article Online

DOI: 10.1039/D5EL00143A

EES Solar ARTICLE

52. M. Fu, X. Shan, S. Wang, X. Zhao, R. Tao, L. You, Z. Deng, X. Fang and G. Meng, *ACS Applied Electronic Materials*, 2024, **6**, 4876-4882.

- 53. Z.-w. Kwang, C.-W. Chang, T.-Y. Hsieh, T.-C. Wei and S.-Y. Lu, *Electrochimica Acta*, 2018, **266**, 118-129.
- 54. T.-W. Ng, C.-Y. Chan, M.-F. Lo, Z. Q. Guan and C.-S. Lee, *Journal of Materials Chemistry A*, 2015, **3**, 9081-9085.
- 55. J. Chen, J. Lv, X. Liu, J. Lin and X. Chen, *Physical Chemistry Chemical Physics*, 2023, **25**, 7574-7588.
- F. Zeng, L. Xu, J. Xing, Y. Wu, Y. Zhang, H. Zhang, C. Hu, B. Dong, X. Bai and H. Song, *Advanced Science*, 2024, 11, 2404444.

In-depth Investigation of Methylamine Gas Post-treatment for MAPbI₃ Films and its Potential for Upscaling Perovskite Solar Cells View Article Online

DOI: 10.1039/D5EL00143A

Duc-Anh Le, a Tzu-Chien Wei*a,b

- ^{a.} Department of Chemical Engineering, National Tsing Hua University, 101, Sec.2, Guang-Fu Road, Hsinchu, Taiwan 30013, Republic of China.
 - b. Research Center for Critical Issues, Academia Sinica, Tainan, Taiwan, Republic of China.

Data availability statement

The data supporting this article have been included as part of the ESI.† More raw data are available from the corresponding author on reasonable request.